Journal of the Mechanics and Physics of Solids 60 (2012) 1545–1560

Contents lists available at SciVerse ScienceDirect

Journal of the Mechanics and Physics of Solids

journal homepage: www.elsevier.com/locate/jmps

Micromechanical models to guide the development of synthetic 'brick and mortar' composites

Matthew R. Begley [a,*], Noah R. Philips [a], Brett G. Compton [a], David V. Wilbrink [b], Robert O. Ritchie [c], Marcel Utz [d]

[a] University of California, Santa Barbara CA 93106, United States
[b] Eindhoven University of Technology, the Netherlands
[c] University of California, Berkeley, CA 94720, United States
[d] University of Virginia, Charlottesville, VA 22902, United States

ARTICLE INFO

Article history:
Received 4 November 2011
Received in revised form
22 January 2012
Accepted 3 March 2012
Available online 10 March 2012

Keywords:
Composites
Micromechanics
Strength
Modulus
Nacre

ABSTRACT

This paper describes a micromechanical analysis of the uniaxial response of composites comprising elastic platelets (bricks) bonded together with thin elastic perfectly plastic layers (mortar). The model yields closed-form results for the spatial variation of displacements in the bricks as a function of constituent properties, which can be used to calculate the effective properties of the composite, including elastic modulus, strength and work-to-failure. Regime maps are presented which indicate critical stresses for failure of the bricks and mortar as a function of constituent properties and brick architecture. The solution illustrates trade-offs between elastic modulus, strength and dissipated work that are a result of transitions between various failure mechanisms associated with brick rupture and rupture of the interfaces. Detailed scaling relationships are presented with the goal of providing material developers with a straightforward means to identify synthesis targets that balance competing mechanical behaviors and optimize material response. Ashby maps are presented to compare potential brick and mortar composites with existing materials, and identify future directions for material development.

1. Introduction

The surprising strength and ductility of nacre (in light of its largely inorganic composition Jackson et al., 1988) can be attributed to its unique microstructure, which consists of precisely aligned ceramic platelets (bricks) bonded together with an extremely thin organic layer (mortar). Though the microstructure and associated deformation mechanisms involve many intricacies (see review in Espinosa et al., 2009), the underlying composites concept is arguably straightforward (e.g. Jackson et al., 1988; Espinosa et al., 2009; Jager and Fratzl, 2000; Currey et al., 2001; Evans et al., 2001; Gao et al., 2003; Ji and Gao, 2004a,b; Barthelat et al., 2006; Tang et al., 2007; Rabiei et al., 2010; Wang and Boyce, 2010; Zhang et al., 2010, 2011): (i) high composite stiffness is maintained by severely limiting the volume fraction of the compliant ductile phase (on the order of several percent or less), (ii) high composite strength is achieved by utilization of small volumes of the ceramic phase (i.e. strong bricks), combined with thin mortar sections and an interlocking brick architecture to efficiently

* Corresponding author. Tel.: +1 805 679 1122.
E-mail address: begley@engr.ucsb.edu (M.R. Begley).

0022-5096/$ - see front matter © 2012 Elsevier Ltd. All rights reserved.
doi:10.1016/j.jmps.2012.03.002

concentrate loads onto the bricks via shear transfer, and (iii) ductility is promoted by brick pull-out, which can alternatively be thought of as micro-cracking in the composite that diffuses damage.

While this underlying composite concept may be straightforward, it is also clear that there are competing deformation mechanisms that lead to trade-offs in macroscopic composite performance (e.g. Ji and Gao, 2004a; Rabiei et al., 2010; Wilbrink et al., 2010). For instance, an increase in the peak shear stress that can be carried by the mortar (or sliding interfaces) can produce an increase in the composite strength, but can also lead to a decrease in composite ductility (by preventing sliding prior to brick failure) (Ji and Gao, 2004a; Wilbrink et al., 2010). The transition between these two mechanisms (mortar failure vs. brick failure) depends not only on the peak shear stress carried by the mortar, but also on the brick size (which dictates brick stress) and mortar thickness (which dictates mortar strain for a given composite strain). Ji and Gao (2004a) and Wilbrink et al. (2010): this implies there is an optimal yield stress for a given geometry, or conversely, an optimal geometry for a given mortar yield stress.

In the development of synthetic 'brick and mortar' materials (Munch et al., 2008; Tang et al., 2003; Launey et al., 2009; Ekiz et al., 2009; Kakisawa et al., 2010; Launey et al., 2010; Posiadlo et al., 2007; Bonderer et al., 2008, 2010a,b), such considerations are tantamount to the criteria that define effective processing pathways. The selection of constituent materials determines the desired geometry that serves as a target for process refinement. Alternatively, the limits of a given processing route should inform materials selection (provided, of course, the processing route allows for alternatives). Quantitative connections between constituent properties, brick architecture and macroscopic composite response are thus critical to synthetic materials development. Given the currently uncertain limits on microstructures accessible through synthesis techniques under development (Munch et al., 2008; Tang et al., 2003; Ekiz et al., 2009; Kakisawa et al., 2010; Posiadlo et al., 2007; Bonderer et al., 2010a), and the desirability of utilizing a wide range of materials, analytical models that make such connections are highly desirable, since they neatly side-step the need for a cumbersome numerical study that covers a broad parameter space.

This is the focus of the present work, rather than an explicit treatment of nacre or an attempt to quantify deformation mechanisms in natural materials. (It is worth noting that the mechanisms at work in natural materials may be far more complex than synthetics (e.g. Jackson et al., 1988; Espinosa et al., 2009; Jager and Fratzl, 2000; Currey et al., 2001; Evans et al., 2001; Gao et al., 2003; Ji and Gao, 2004a,b; Barthelat et al., 2006; Tang et al., 2007; Rabiei et al., 2010; Wang and Boyce, 2010), and exploit additional beneficial microstuctural features such as hierarchy at multiple scales Zhang et al., 2011.) The present analytical models describe the macroscopic modulus, strength and ductility of an idealized composite (see Fig. 1), with elastic bricks arranged in a staggered pattern that are bonded with elastic–perfectly plastic mortar. Synthetic brick and mortar materials use glassy polymers or ductile metals as mortar (Munch et al., 2008; Kakisawa et al., 2010; Launey et al., 2010; Bonderer et al., 2008, 2010a); both are well-represented by an elastic–perfectly plastic solid. (In addition, this type of approximation is fairly general and may accurately reflect behaviors for a variety of mechanisms such as frictional sliding Evans et al., 2001.) To illustrate the implications of materials selection and processing limits, new mechanism maps are presented which illustrate trade-offs in macroscopic properties that are triggered by a transition in failure mechanisms, e.g. brick failure, vertical interface failure and horizontal interface failure. To evaluate the validity of the models, they are used to make comparisons with previous measurements on a $PMMA/Al_2O_3$ synthetic composite (Munch et al., 2008). The model is then used to estimate the range of improvements that are possible (i.e. fabrication targets) for synthetic materials.

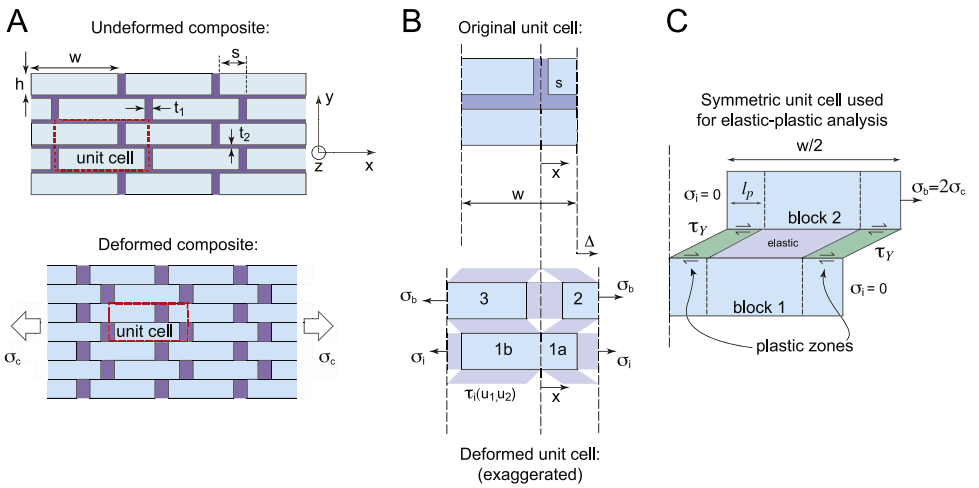

Fig. 1. Schematic illustrations of the idealized composite and unit cell used to derive composite tensile properties: (A) variables defining the geometry, (B) original and deformed unit cells for asymmetric layout analyzed for modulus and strength, and (C) symmetric unit cell analyzed for elastic–plastic behavior.

As with any analysis of an idealized unit cell (see Fig. 1), the model cannot capture localized damage: damage is necessarily assumed to be widespread and approximately uniform. In real materials, the distribution of damage may not be diffuse, particularly for those events that immediately precede macroscopic rupture. Micrographs of failure surfaces in both nacre and synthetic 'brick and mortar' microstructures show such localized damage, manifested as 'brick pull-out', i.e. relative sliding of adjacent bricks (e.g. see review in Espinosa et al., 2009 and micrographs in Munch et al., 2008). These micrographs cannot be representative of diffuse damage in the bricks, for the simple reason that failure strains in these materials are on the order of $\sim 1-3\%$ and moreover, the composites ultimately rupture abruptly with a sharp drop in load. (A possible exception is the synthetic material described in Munch et al., 2008: still, although the composite gradually loses load-bearing capacity after peak stress, failure strains are still $\sim 1-3\%$.) If large-scale sliding corresponding to brick pull-out were widely activated, failure strains would be much larger and one would likely observe concomitant softening behavior. Moreover, characterization techniques that produce broader fields-of-view do show wide-spread damage, such as the micro-crack distributions seen in x-ray tomography scans (Launey et al., 2009). Such damage events more than likely precede the emergence of dominant flaw that would dramatically reduces the average stress for a given level of macroscopic strain. Hence, it is reasonable to believe that the essential elements of the stress–strain behavior can be rationalized with a diffuse damage model, provided the model's predictions for macroscopic failure strain, are in agreement with observations. As will be illustrated, even if rupture strains in the mortar are large (say $\sim 100\%$), the present models still predict failure strains in the 1–3% range.

The models presented here draw inspiration from many previous works, which have utilized a similar idealized geometry and analysis approach, such as Jager and Fratzl (2000), Evans et al. (2001), Ji and Gao (2004a,b), and Wilbrink et al. (2010). Similarly, they build upon previous numerical studies of nacre that have analyzed a more limited parameter space (e.g. Ji and Gao, 2004b; Tang et al., 2007; Barthelat et al., 2007). In addition, the models (though not the motivating microstructures) naturally bear resemblance to shear-lag models developed for short-fiber composites (e.g. see Tucker and Liang, 1999; Nairn, 1997 and references therein) and for thin films (Hu and Evans, 1989), which are often geared towards capturing shear transfer between adjacent whiskers/films. The important distinction from previous purely analytical models (as opposed to numerical results) is that the present models include *all* of the following: (i) bricks are perfectly aligned yet can have an arbitrary off-set from row to row, (ii) very small volume fractions of mortar that exhibit elastic behavior up to a critical stress, (iii) the vertical interfaces carry load up to a specified rupture strain, and (iv) the relative slip between bricks and brick displacements varies spatially in the loading direction. With regard to the latter effect, the model in Zhang et al. (2010) comes closest, but does not consider the effect of bonding between brick ends. This will be demonstrated to be critical for proper calculation of the composite modulus and failure of vertical interfaces. Further, we demonstrate that even for an elastic–perfectly plastic mortar, geometric hardening occurs such that it takes increasing load to propagate the plastic zone in the horizontal mortar sections. While some of these effects have been treated in previous studies, all are needed together for a single model to paint a complete picture of composite response.

For example, without including the effect of load-bearing vertical interfaces and elasticity in the bricks, the stress distribution in the bricks and hence the composite failure stress cannot be calculated in this regime. Whether or not the brick ends remain bonded is a critical question in materials development, as debonding at these interfaces prior to brick failure is critical to achieve toughness (e.g. Espinosa et al., 2009; Ji and Gao, 2004a,b; Barthelat et al., 2006; Zhang et al., 2010). Previous experiments with synthetic materials have demonstrated that increases in material interface strength can improve aspects of mechanical performance (e.g. Tang et al., 2003). However, for some material systems there is likely an upper limit on interface strength that still ensures ductility, which can be identified with the present models. Thus, for design and synthesis purposes (as opposed to analysis of existing materials), a model is required that spans the *full* range of composite behavior, such that trade-offs between the effective modulus, strength and ductility can be explicitly quantified. The explicit inclusion of *all* the effects described above enable the construction of failure mechanism maps that indicate regimes of composite behavior as a function of constituent properties, which are not possible with previous models.

2. Elastic modulus and strength for brittle materials

The idealized composite geometry is shown in Fig. 1. The wallpaper symmetry group is *pmm*, with two bricks per unit cell, which are separated by one brick height vertically, and shifted by s horizontally. For $s=w/2$, the symmetry increases to *cmm*. The mortar thickness is assumed to be small in comparison to the brick dimensions: t_1 is the thickness of the vertical mortar sections ($z-y$ and $x-y$ planes), and t_2 is the thickness of the horizontal mortar sections ($x-z$ plane). It assumed that the components deform only in the x-direction: as such, the arrangement of the bricks in the through-thickness direction (i.e. whether or not they overlap in adjacent $x-z$ planes) does not factor into the response. Assuming approximately square bricks in the $x-z$ plane of dimension w, and small mortar thickness such that $t_1, t_2 \ll w, h$, the volume fraction of the mortar phase is given by

$$f = \frac{t_1}{w} + \frac{t_2}{h} + \frac{t_1}{w} = \bar{t}\left(\frac{2\alpha+\overline{w}}{\overline{w}}\right) \tag{1}$$

where $\overline{t}=t_2/h$, $\overline{w}=w/h$ are the aspect ratio of the bricks, and $\alpha=t_1/t_2$ is the ratio of thickness of vertical and horizontal mortar sections. For uniform mortar thickness $f=\overline{t}(2+\overline{w})/\overline{w}$, while for very large aspect ratios $f\sim\overline{t}$ since horizontal interfaces are dominant.

Small plane strain deformations are assumed with zero strain in the z-direction, and zero stress in the y-direction. Under uniaxial deformation, the horizontal interfaces experience pure shear according to the relative displacements between adjacent bricks in different rows, while the vertical interfaces experience pure tension according to the relative displacements between adjacent bricks in the same row. The mortar is presumed to be thin enough such that horizontal mortar layers experience uniform shear strains. The bricks are assumed to be perfectly elastic, while the mortar is considered to be elastic–perfectly plastic and characterized by the uniaxial yield strength σ_Y.

In this section, results are presented for fully elastic response of both constituents, with the yield strength of the mortar used to define the elastic limit. It is assumed that interface rupture occurs immediately after yielding, such that brick failure or horizontal failures correspond to composite failure. In contrast, the composite may or may not still carry load after failure of the vertical interfaces. Ductile (post-yielding) behavior is considered in Section 3.

2.1. Governing equations for asymmetric overlap

The bricks are numbered as shown in Fig. 1B. Two solutions are needed for displacements in brick *#1*, since the relative displacements will be different on either side of the origin: here, the displacement of brick *#1* for $x>0$ is denoted as $u_{1a}[x]$, while the displacements for $x<0$ is denoted as $u_{1b}[x]$. Continuity dictates $u_{1a}[0]=u_{1b}[0]$. The macroscopic strain in the composite, ϵ_c, is dictated by the displacements of the ends of bricks *#2* and *#3* relative to the width of the unit cell: that is, $w\cdot\epsilon_c=u_2[s]-u_3[-(w-s)]$. In the following, the position is normalized by the brick width, $\overline{x}=x/w$ while the displacements are normalized according to $\overline{u}=u/(w\epsilon_b^f)$, where ϵ_b^f is the failure strain in the bricks. This notation leads to the following complete set of governing equations:

$$\overline{u}_{1a}''=2\kappa_2^2(\overline{u}_2-\overline{u}_{1a}),\quad 0<\overline{x}<\overline{s}$$

$$\overline{u}_{1b}''=-2\kappa_2^2(\overline{u}_3-\overline{u}_{1b}),\quad -(1-\overline{s})<\overline{x}<0 \tag{2}$$

$$\overline{u}_2''=-2\kappa_2^2(\overline{u}_2-\overline{u}_{1a}),\quad 0<\overline{x}<\overline{s}$$

$$\overline{u}_3''=2\kappa_2^2(\overline{u}_3-\overline{u}_{1b}),\quad -(1-\overline{s})<\overline{x}<0 \tag{3}$$

where $\overline{s}=s/w$ (i.e. the normalized shift in alignment from row to row), and κ_2 is a dimensionless parameter that describes the strength of shear transfer in the horizontal mortar sections, given by

$$\kappa_2=\sqrt{\frac{(1-\nu_m)\overline{E}_m w^2}{2\overline{E}_b t_2 h}} \tag{4}$$

where $\overline{E}_m=E_m/(1-\nu_m^2)$ is the plane-strain modulus of the mortar (with E_m as the elastic modulus of the mortar, and ν_m is Poisson's ratio of the mortar), $\overline{E}_b=E_b/(1-\nu_b^2)$ is the plane strain modulus of the mortar (with E_b as the elastic modulus of the bricks and ν_b is Poisson's ratio of the bricks). The corresponding boundary (and symmetry) conditions are given by:

$$\overline{u}_{1a}[0]=\overline{u}_{1b}[0]=0,\quad \overline{u}_2[\overline{s}]=\overline{\Delta},\quad \overline{u}_2[\overline{s}]-\overline{u}_3[-(1-\overline{s})]=\overline{\epsilon}_c$$

$$\overline{u}_3'[0]=\overline{u}_2'[0]=\kappa_1(\overline{u}_2[0]-\overline{u}_3[0]),\quad \overline{u}_1'a[\overline{s}]=\overline{u}_{1b}'[-(1-\overline{s})],\quad \overline{u}_1'[0]=\overline{u}_2'[\overline{s}]=u_3'[-(1-\overline{s})] \tag{5}$$

where $\overline{\epsilon}_c=\epsilon_c/\epsilon_b^f$ represents the total strain imposed on the unit cell normalized by the brick failure strain, and κ_1 is a dimensionless parameter that describes the strength of direct stress transfer in the vertical mortar sections, and is given by:

$$\kappa_1=\frac{\overline{E}_m w}{\overline{E}_b t_1} \tag{6}$$

The displacement $\overline{\Delta}=\Delta/(w\epsilon_b^f)$ represents the dimensionless displacement of the symmetry boundary of brick *#2*: this unknown constant can be determined by adding $\overline{\Delta}'[\overline{x}]=0$ to the list of equations. Thus, in total, there are four coupled second order differential equations and one first order differential equation, requiring the nine boundary conditions, given as Eq. (5). Note that the horizontal and vertical interface behaviors are decoupled in the sense that different constitutive laws could be used for each one. This includes the limit where the vertical interfaces carry no load (e.g. are pre-cracked), in which case $\kappa_1=0$.

Once the solution is obtained, the maximum stress in the bricks, the maximum shear stress in the horizontal interface, and the stress in the vertical interfaces is found via:

$$\overline{\sigma}_b\equiv\frac{\sigma_b}{\sigma_b^f}=\overline{u}_1'[0],\quad \overline{\tau}_i\equiv\frac{\tau}{\sigma_b^f}=2\kappa_2^2\left(\frac{h}{w}\right)\overline{u}_2[0],\quad \overline{\sigma}_i\equiv\frac{\sigma_i}{\sigma_b^f}=\overline{u}_2'[0] \tag{7}$$

where $\sigma_b^f = \overline{E}_b \epsilon_b^f$ is the failure stress of the bricks. The composite stress is given by the average of the peak stress in the bricks and the stress in the vertical interfaces:

$$\overline{\sigma}_c \equiv \frac{\sigma_c}{\sigma_b^f} = \frac{1}{2}(\overline{u}_1'[0] + \overline{u}_2'[0]) \tag{8}$$

Note that the shear stress depends on the parameter h/w in addition to $\kappa_{1,2}$, whereas the composite modulus, brick stress and vertical interface stress depend only on $\kappa_{1,2}$.

2.2. Purely elastic solutions

The full solutions to the equations outlined above are cumbersome, but can be trivially recovered using *Mathematica* or the like. The displacement results will scale linearly with the strain applied to the unit cell as required. The effective modulus of the elastic composite is defined according to $\sigma_c = \overline{E}_c \cdot \overline{\epsilon}_c$, and is given by

$$\overline{E}_c = \frac{\overline{E}_c}{\overline{E}_b} = \frac{2(\sinh[\kappa_2]\kappa_1 - 2\sinh[(-1+\overline{s})\kappa_2]\sinh[\overline{s}\kappa_2]\kappa_2)}{2\sinh[\kappa_2](1+\kappa_1) + (\cosh[\kappa_2] - \cosh[(-1+2\overline{s})\kappa_2])\kappa_2} \tag{9}$$

The peak stresses in the constituents are given by

$$\overline{\sigma}_b = \frac{2(\sinh[\kappa_2]\kappa_1 - 2\sinh[(-1+\overline{s})\kappa_2]\sinh[\overline{s}\kappa_2]\kappa_2)}{2\sinh[\kappa_2](1+\kappa_1) + (\cosh[\kappa_2] - \cosh[(-1+2\overline{s})\kappa_2])\kappa_2} \cdot \overline{\epsilon}_c \tag{10}$$

$$\overline{\tau}_i = -\frac{4\cosh[\overline{s}\kappa_2]\sinh[(-1+\overline{s})\kappa_2]\kappa_2^2}{2\sinh[\kappa_2](1+\kappa_1) + (\cosh[\kappa_2] - \cosh[(-1+2\overline{s})\kappa_2])\kappa_2} \cdot \frac{h}{w} \cdot \overline{\epsilon}_c \tag{11}$$

$$\overline{\sigma}_i = \frac{2\sinh[\kappa_2]\kappa_1}{2\sinh[\kappa_2](1+\kappa_1) + (\cosh[\kappa_2] - \cosh[(-1+2\overline{s})\kappa_2])\kappa_2} \cdot \overline{\epsilon}_c \tag{12}$$

Again, note that the peak shear stress in the bricks involves a fundamentally different scaling than the modulus and direct stresses (which depend only on $\kappa_{1,2}$) through the factor h/w. Also, these results are valid when $\kappa_1 = 0$. This limit represents the composite response after rupture of the vertical sections (or a layered composite with a regular periodic array of cracks). For a purely elastic system, the stress in the composite after vertical cracking is simply $\sigma_c = \overline{E}_c(\kappa_1 = 0) \cdot \epsilon$. Hence, the stress drop upon vertical cracking is $\Delta\sigma_c = (\overline{E}_c - \overline{E}_c(\kappa_1 = 0))\epsilon_c$, where the composite strain ϵ_c is taken to be the composite strain at which the vertical interface fails.

2.3. Composite elastic modulus

With regard to purely elastic behavior, there are several other asymptotic limits that are of interest. As a check of the validity of Eq. (9), consider the limits that $\overline{s} \to 0$ or $\kappa_2 \to 0$: in these limits shear transfer between the bricks is zero and one should recover the stiffness of two linear springs in series (i.e. bricks separated by thin vertical sections of mortar) thickness. These asymptotic limits yield:

$$\overline{E}_c \approx \frac{\kappa_1}{1+\kappa_1} = \frac{\overline{E}_m w}{\overline{E}_b t_1 + \overline{E}_m w} \tag{13}$$

which is indeed the correct form assuming that there are two springs in series. The other two limits pertain to small or large values of κ_1 and κ_2^2. For $\kappa_1 \ll 1$ and $\kappa_2^2 \ll 1$, an asymptotic expansion of Eq. (9) yields the following approximation:

$$\overline{E}_c \approx \kappa_1 + 2\kappa_2^2 \cdot (\overline{s} - \overline{s}^2) \tag{14}$$

Immediately one observes that the maximum stiffness corresponds to brick overlap of one-half their width, $\overline{s} = 1/2$. Since the κ values are presumed small, this equation is only valid in the limit that the observed composite modulus is much lower than that of the bricks, i.e. when $\overline{E}_c/\overline{E}_b \ll 1$.

This is not the case for the synthetic composites pursued elsewhere, nor for natural nacre. To see this, recast the κ values as follows:

$$\kappa_1 = \frac{\overline{E}_m}{f\overline{E}_b} \cdot \frac{2\alpha + \overline{w}}{\alpha}$$

$$\kappa_2^2 = \frac{\overline{E}_m}{f\overline{E}_b} \cdot \frac{(1-\nu_m)}{2} \cdot \overline{w}(2\alpha + \overline{w}) \tag{15}$$

where f is the volume fraction of the mortar phase. Consider, for example, a mortar to brick modulus ratio of $\overline{E}_m/\overline{E}_b \sim 10^{-3}$, volume fractions of $f \sim 0.01$, brick sizes of $\overline{w} = 5$, $\nu_m \sim 1/3$ and uniform mortar ($\alpha = 1$): then, $\kappa_1 \sim 0.7$ and $\kappa_2^2 \sim 1$. Clearly, these are not negligible compared to unity, and moreover, κ_1 and κ_2^2 are comparable. Even for relatively long bricks, the normal stiffness still plays a significant role. Simply put, the limit of small mortar volume fraction corresponds to large

values of κ. To obtain a simplified expression for large values of κ, note that $\sinh[x] \approx \cosh[x] \approx (1/2)e^x$ in the limit of large x. Then, for large κ and $\overline{s} = 1/2$, Eq. (9) reduces to

$$\overline{E}_c \approx \frac{2\kappa_1 + \kappa_2}{2(1+\kappa_1)+\kappa_2}, \quad \kappa_{1,2} \geq 1 \tag{16}$$

This scaling implies that this is the proper approximation when $\overline{E}_c \sim \overline{E}_b$, i.e. when the composite modulus is close to that of just the bricks.

A key insight from the above equations is that it is difficult to anticipate effective composite behavior for materials with extreme modulus mismatch and small volume fractions, since the volume fraction and modulus mismatch have off-setting effects. This implies that when considering a range of brick sizes, say $2 < \overline{w} < 15$ (as in Fig. 2), the κ will span both limits! Hence, the asymptotic expansions may be of limited utility, except in extreme limits of very low composite modulus or that close to the bricks themselves. Put another way, both the mortar deformation and brick deformation are important, regardless of the fact that the mortar has far smaller volume fraction and far smaller stiffness. This has critical implications for predicting the initial damage events in the composite (which occur at the limit of elasticity in the components), as it implies that deformation in both constituents must be properly addressed.

The elastic modulus of the composite, normalized by the brick modulus, is shown in Fig. 2 as a function of brick aspect ratio (for fixed volume fraction) and as a function of volume fraction (for fixed brick aspect ratio). The symmetric case $\overline{s} = 1/2$ is shown. The solid lines correspond to moduli with intact vertical interfaces, the dashed line corresponds to moduli with cracked vertical interfaces. To generate the plot, the definitions in Eq. (15) are used for $\kappa_{1,2}$. As expected, increasing the brick aspect ratio increases the composite modulus, as does decreasing the volume fraction of the mortar: in the limits of zero volume fraction recovers the elastic modulus of the bricks.

In the limit of infinite brick size, one again recovers the elastic modulus of the bricks: this is a consequence of the assumption that the mortar experiences pure shear. For extremely long bricks and intact vertical interfaces – *i.e.* the lamellar limit – the mortar will actually stretch axially with the bricks and carry load in proportion to its volume fraction. This effect is not recovered in the present model, and thus the model does not recover the expected results for lamellae in that limit. However, the discrepancy between the present limit and the rule-of-mixtures lamellae limit is on the order of fE_m/E_b, presumably a very small fraction for compliant mortar and/or small volume fractions.

It is worth emphasizing that even with extreme modulus mismatch, small volume fractions, and very long bricks, the vertical interfaces play a significant role in the composite modulus. Cracking of vertical interfaces leads to dramatic reduction in stiffness. Though not shown, the effect is even more dramatic when the layout is not symmetric.

2.4. Brittle composite strength

The composite strength can be evaluated by using the elastic results to predict the stress required to trigger various failure sequences. For brittle materials, brick failure or horizontal shear failure corresponds to material rupture. The composite can still carry load after vertical failure, such that the strength is dictated by the stress required to subsequently yield the horizontal interface, or break the bricks.

A summary of the possible failure sequences is shown schematically in Fig. 3. The stress required for a specific failure event is found by equating the associated stress with the material strength and solving for the composite strain ϵ_c required for that event. The composite stress is then the critical strain multiplied by the relevant composite modulus (e.g. $\overline{E}_c(\kappa_1 \to 0)$

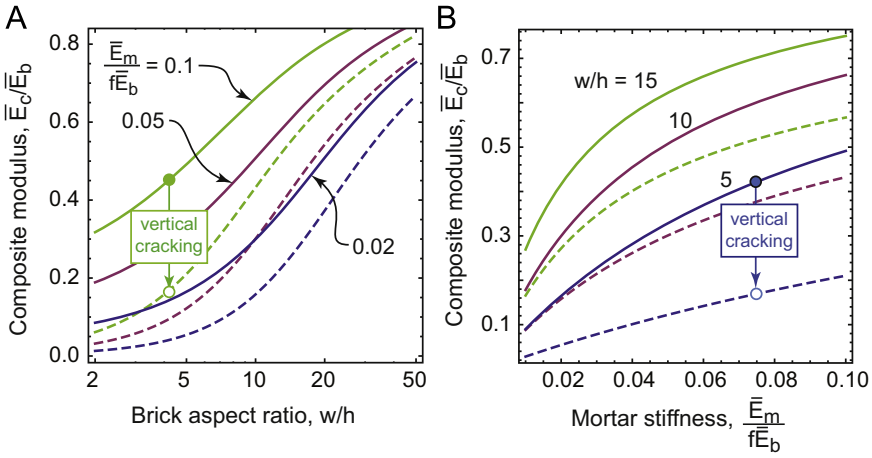

Fig. 2. (A) Composite modulus as a function of brick aspect ratio. (B) Composite modulus as a function of the relative stiffness parameter (or volume fraction for fixed modulus ratio). In both figures, solid lines are for intact vertical interfaces, while dashed lines are the modulus after vertical failure.

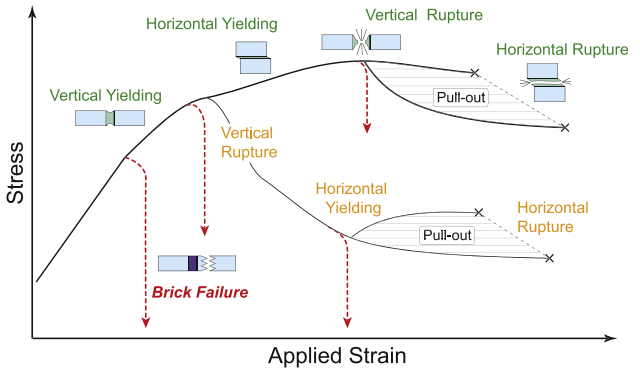

Fig. 3. Schematic illustration of the possible failure sequences in brick and mortar composites: the desired path is highlighted in green, which corresponds to strong, stiff, ductile materials. (For interpretation of the references to color in this figure legend, the reader is referred to the web version of this article.)

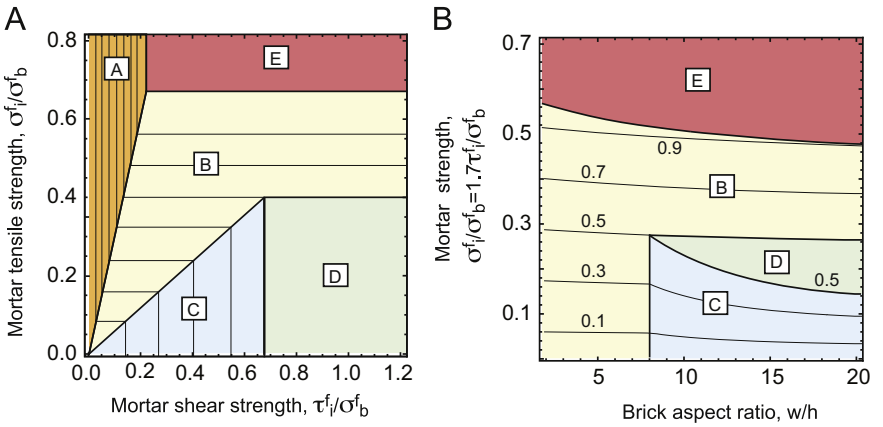

Fig. 4. Contours maps of composite stress at the elastic limit (i.e. the stress associated with the onset of yielding), $\sigma_c^f = \sigma_b^f$ (increments of 0.1), with shaded regions indicating failure sequence: (A) horizontal yielding initiates first, (B) vertical failure followed by immediate brick failure, (C) vertical yielding followed by horizontal yielding, (D) vertical failure followed by brick failure, (E) brick failure controls strength. Part (A) shows contours for different combinations of vertical and horizonal mortar strengths for $w/h=5$, while part (B) shows contours for a fixed ratio of interface strengths.

if the vertical interfaces have failed). The peak stress can be calculated using the following algorithm:

- Calculate the composite stresses corresponding to brick failure $\overline{\sigma}_c^{BF}$, horizontal interface failure, $\overline{\sigma}_c^{HF}$, and vertical interface failure $\overline{\sigma}_c^{VF}$. If either of the first two are the minimum, this represents the composite strength.
- If the vertical interfaces fail at the minimum stress, set $\kappa_1 \to 0$ and calculate the composite stress required for horizontal interface failure (with the vertical interfaces removed), σ^{VFHF}. If $\overline{\sigma}^{VFHF} \geq 1/2$, brick failure occurs prior to horizontal interface yielding, since the stress on the bricks is $2\sigma_c$; hence, the second failure event occurs at $\mathrm{Min}[\overline{\sigma}^{VFHF}, 1/2]$.
- Check to see if the second failure event occurs at a higher stress than the first (i.e. vertical interface failure): if not, either the bricks fail or the horizontal interface yields immediately upon vertical interface failure, such that vertical interface failure represents the peak allowable stress.

Strictly speaking, when the interfaces are ductile, the composite stress required for failure of the horizontal interfaces (assuming vertical interface failure has occurred) is dictated by the pull-out stress, given by $\sigma_c = \tau_Y w/(4h)$, where τ_Y is the shear yield stress of the mortar. (Once the vertical interfaces have failed, the composite stress depends only on the stress in the bricks at the origin (see Fig. 1), which is dictated by uniform shear stress along its length: the mortar volume fraction will influence the strain at which horizontal interface yielding occurs, but not the stress.) However, as will be shown in the next section, the stress associated with the onset of yielding (as predicted by the elastic analysis in this section) is a fair approximation to the peak stress in the composite. In essence, the increase in stress required to propagate the plastic zone is rather modest, such that the elastic limit is often very close to the pull-out stress. This is demonstrated in Section 3.

Fig. 4A shows contours of the composite strength (determined via the above algorithm), as a function of the critical failure stresses of the horizontal and vertical interfaces. In order to separate the roles of brick aspect ratio, mortar volume fraction and relative thickness of the interfaces, the dimensionless stiffness parameters are recast according to Eq. (15).

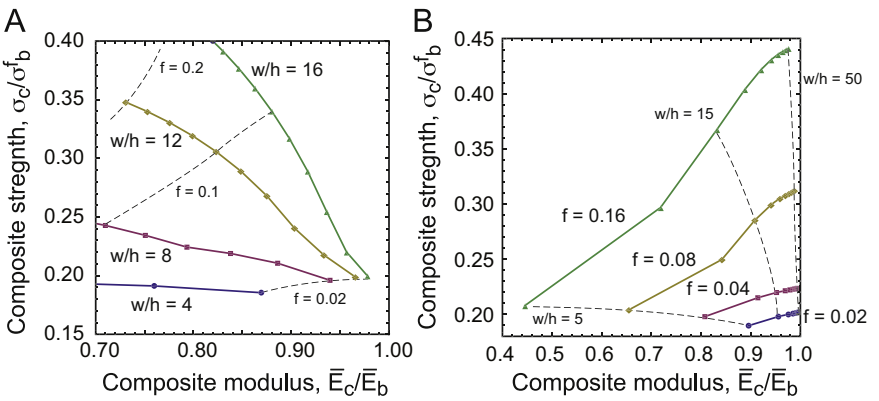

Fig. 5. Relationship between composite strength and modulus as a function of brick size and volume fraction: in part (A), the brick size is fixed for each curve (w/h=4,8,12,16), while the mortar volume fraction is stepped from f=0.2 to f=0.02 in increments of $\Delta f = 0.02$. In part (B), the volume fraction is fixed for each curve f=0.02, 0.04, 0.08, 0.16, while the brick size is stepped from w/h=5 to w/h=50 in increments of $\Delta w/h = 5$. The modulus ratio is taken as $E_m/E_b = 1/75$, while the mortar strength is $\tau_Y = 0.15\sigma_b^f$.

Here, $\nu_m = 1/3$ is assumed. The boundaries in Fig. 4 illustrate the failure mechanism controlling strength. In region A, the mortar shear strength is insufficient to prevent horizontal rupture as the initial event, and this mechanism controls composite strength. In region B, the vertical interfaces fail first at a stress that is higher than that required to crack the bricks or yield the horizontal interfaces: i.e. vertical failure yields immediately to composite failure. In region C, the vertical interfaces fail first, followed by delayed shear failure of the horizontal interface (at a stress higher than that required for the initial cracking of vertical interfaces). In region D, the vertical interfaces fail first, then the bricks: the composite strength is the maximum possible with failed vertical interfaces, i.e. one-half the brick strength. In region E, the mortar is strong enough to fail the bricks as the initial event, and as such, the composite strength is constant and independent of the mortar strength.

Fig. 4B shows contours of composite strength as a function of mortar strength and brick aspect ratio, assuming interface failure stresses given by $\tau_i^f = \sigma_i^f/\sqrt{3}$ (as consistent with a Von Mises yield criterion). Here, the vertical mortar sections are set to have one-tenth the thickness of the horizontal mortar sections, i.e. $\alpha = 0.1$, in order to ensure that the most of the same regimes seen in Fig. 4A also appear in Fig. 4B. Though not shown, for equal mortar thickness in the horizontal and vertical interfaces, vertical interfaces always fail first provided $\sigma_i^f < 3.7\tau_i^f$. This implies vertical interface failure is always the initial damage event (in particular for Von Mises plasticity), barring unusual differences between the strength of the mortar sections.

Fig. 5 shows the relationships between composite modulus and composite strength, for a fixed interface strength, $\sigma_i^f = \tau_i^f = 0.15\sigma_b^f$, and modulus ratio, $\bar{E}_m/\bar{E}_b = 1/75$. Along a given curve in Fig. 5A, the brick sizes are held fixed to $w/h = 4, 8, 12, 16$, while the volume fraction is varied from f=0.02 to f=0.2 in steps of $\Delta f = 0.02$. In Fig. 5B, the volume fraction is held fixed to $f = 0.02, 0.04, 0.08, 0.16$ while the brick sizes are varied from $w/h = 5$ to $w/h = 50$ in steps of $\Delta(w/h) = 5$. For fixed brick size, decreasing the volume fraction corresponds to making the mortar sections thinner: this has the effect of making them stiffer, but also subject to higher stresses: hence, strength drops while modulus increases. Conversely, for fixed volume fraction, increasing the aspect ratio of the bricks corresponds to thicker mortar sections. Importantly, both modulus and strength increase with brick size for fixed volume fraction: this is because (a) the mortar sections are getting thicker, increasing the applied strain required to cause them to fail, while (b) shear transfer between bricks is more efficient. These results emphasize the importance of simultaneously controlling volume fraction and brick aspect ratio: without such control, gains due to increase in aspect ratio can be off-set by losses due to higher volume fractions.

3. Ductility: elastic–plastic response with cracked vertical interfaces

For simplicity's sake, results are presented for a symmetric brick layout ($\bar{s} = 1/2$) with failed vertical interfaces. This implies symmetric plastic zones that extend from the edges of the bricks inwards. (The elastic solution presented earlier can be used to verify that peak shear stresses occur at the edges of the bricks.) The model consists of one-half of the bottom brick (#1), which is fixed at x=0, with one-half of the top brick (#2), which displaces laterally. The brick is divided into three geometric zones: two zones with yielded interfaces and one zone with an elastic interface, as shown in Fig. 1C.

3.1. Governing equations

As before, let $\bar{x} = x/w$, such that the domain is $0 < \bar{x} < \frac{1}{2}$; this avoids confusion later when expressing the results in terms of the brick aspect ratio, $\bar{w} = w/h$. The size of the plastic zone ℓ_p is normalized according to $\bar{\ell}_p = \ell_p/w$, such that its

maximum value is $\frac{1}{4}$. Normalize displacements as $\overline{u}_i = u_i/(w \cdot \epsilon_b^f)$, where ϵ_b^f is the failure strain of the bricks: this dictates that the strains in the problem are normalized by the brick failure strain, and the stresses are normalized by the brick failure stress. The problem statement becomes

$$\overline{u}_1''(\overline{x}) = -2\kappa_2^2 \cdot (\overline{u}_2(\overline{x}) - \overline{u}_1(\overline{x})), \quad \overline{\ell}_p < \overline{x} < \tfrac{1}{2} - \overline{\ell}_p \tag{17}$$

$$\overline{u}_2''(\overline{x}) = 2\kappa_2^2 \cdot (\overline{u}_2(\overline{x}) - \overline{u}_1(\overline{x})), \quad \overline{\ell}_p < \overline{x} < \tfrac{1}{2} - \overline{\ell}_p \tag{18}$$

where κ_2 is given by Eq. (4), as before. The boundary conditions are given by

$$\overline{u}_1(0) = 0, \quad \overline{u}_2(\tfrac{1}{2} - \overline{\ell}_p) = \overline{\Delta} \tag{19}$$

$$\overline{u}_2'(\overline{\ell}_p) = \Sigma_Y \cdot \overline{\ell}_p, \quad \overline{u}_1'(\tfrac{1}{2} - \overline{\ell}_p) = \Sigma_Y \cdot \overline{\ell}_p \tag{20}$$

where the normalized shear yield stress of the mortar is given by

$$\Sigma_Y \equiv \frac{\tau_Y w}{\sigma_b^f h} \tag{21}$$

The boundary conditions on displacement gradients arise from force balance at the edges of the plastic zone (the left edge on brick #2, the right edge of brick #1), where the brick stress is given by $\sigma_b = \tau_Y \cdot \ell_p$.

The variable $\overline{\Delta}$ represents the displacement at the elastic–plastic boundary on the right, and is a variable to be determined from the solution. $\overline{\Delta}$ can be related to the macroscopic strain applied to the composite by the relationship:

$$\begin{aligned} \overline{\epsilon}_c &= 2\overline{u}_2(\tfrac{1}{2}) = 2\overline{u}_2(\tfrac{1}{2} - \overline{\ell}_p) + 2\overline{\delta}_p \\ &= 2\overline{\Delta} + 4\overline{\sigma}_c \cdot \overline{\ell}_p - \overline{\Sigma}_Y \ell_p^2 \end{aligned} \tag{22}$$

where $\overline{\delta}_p$ represents the displacement of the right end of the brick *relative to the position* $\overline{x} = 1/2 - \overline{\ell}_p$. $\overline{\delta}_p$ can be determined from a shear lag analysis of the yielded region.

The edge of the plastic zone is determined from the condition that the shear strain at the elastic–plastic boundary is equal to the shear yield strain, γ_Y. In terms of dimensionless variables, this implies:

$$\overline{u}_2(\overline{\ell}_p) - \overline{u}_1(\overline{\ell}_p) = \frac{\gamma_Y \cdot t}{\epsilon_b^f \cdot w} = \overline{\gamma}_Y = \frac{\Sigma_Y}{2\kappa^2} \tag{23}$$

The parametric identity listed last in the above equation is particularly important, since it illustrates the scaling of the normalized shear yield strain. The composite stress is given by

$$\overline{\sigma}_c = \tfrac{1}{2}(\overline{u}_2'(\tfrac{1}{2} - \overline{\ell}_p) + \Sigma_Y \cdot \overline{\ell}_p) \tag{24}$$

Finally, the maximum shear strain in the mortar is given by

$$\overline{\gamma}_{max} \equiv \frac{\gamma_{max} t}{\epsilon_b^f w} = \overline{u}_2(\overline{\ell}_p) - \frac{1}{2}\Sigma_Y \overline{\ell}_p^2 \tag{25}$$

These equations (with the displacement solutions to the differential equations stated above) provide the basis to eliminate $\overline{\ell}_p$ and $\overline{\Delta}$ from the analysis. Solving the above problem with $\overline{\ell}_p = 0$ yields the full elastic solution: in this case, $\Delta = w\epsilon_c/2$, where ϵ_c is the macroscopic strain applied to the material. To predict the proper failure mechanism in the composite, one must check (at all loading increments) to ensure that the brick stress, $\sigma_b = 2\sigma_c$ is less than the brick failure stress, σ_b^f. Further, mortar rupture occurs when the peak shear strain in the mortar is equal to the rupture shear strain.

3.2. Elastic response: brick failure and the onset of yielding

The elastic behavior (prior to yielding) can be found by solving the above equations with $\overline{\ell}_p = 0$: the results are identical to the elastic analysis given in Section 2 for $\overline{s} = 1/2$ and $\kappa_1 = 0$. The elastic modulus of the composite, defined by $\overline{\sigma}_c = \overline{E}_c \overline{\epsilon}_c$, is given by

$$\overline{E}_c = \frac{\kappa_2}{\kappa_2 + 2\coth\frac{\kappa_2}{2}} \tag{26}$$

The maximum brick stress is given by $\overline{\sigma}_b = \sigma_b/\sigma_b^f = 2\overline{\sigma}_c$. Again, the maximum possible composite strength for a material with cracked vertical interfaces is given by $\overline{\sigma}_c = 1/2$. Thus, the composite stress and strain associated with brick failure in the elastic regime is given by

$$[\overline{\epsilon}_c, \overline{\sigma}_c]_{bf}^e = \left[\frac{1}{2} + \frac{\coth\frac{\kappa_2}{2}}{\kappa_2}, \frac{1}{2}\right] \tag{27}$$

The maximum shear strain in the mortar in the elastic regime is given by

$$(\overline{\gamma}_{max})_e = \frac{1}{1+\kappa_2 \sinh\frac{\kappa_2}{2}} \tag{28}$$

Solving this equation with $\gamma_{max}=\gamma_Y$ predicts the composite strain associated with the onset of yielding, $\overline{\epsilon}_{iy}$. The composite stress and strain associated with the onset of mortar yielding is given by

$$[\overline{\epsilon}_c,\overline{\sigma}_c]_{iy} = \left[\frac{\Sigma_Y}{2\kappa_2^2}\left(2+\kappa_2 \tanh\frac{\kappa_2}{2}\right), \frac{\Sigma_Y}{2\kappa}\cdot \tanh\frac{\kappa_2}{2}\right] \tag{29}$$

Thus, in order for mortar yielding to be relevant, the composite stress/strain associated with yielding must be smaller than that associated with brick failure. This condition is dictated by

$$\frac{\Sigma_Y}{2\kappa_2}\cdot \tanh\frac{\kappa_2}{2} \le \frac{1}{2} \tag{30}$$

3.3. Propagation of the plastic zone

To determine the stress–strain response in the transition regime and avoid numerical root finding, one can proceed as follows: first, one finds the solution for $\overline{u}_1(\Sigma_Y,\overline{\Delta},\overline{\ell}_p)$ and $\overline{u}_2(\Sigma_Y,\overline{\Delta},\overline{\ell}_p)$. Eq. (20) can be used to solve for the analytic function $\overline{\Delta}(\Sigma_Y,\Gamma_Y,\overline{\ell}_p)$. One can then generate the stress–strain curve using $\overline{\ell}_p$ as an implicit parameter. That is, one can specify $\overline{\ell}_p$, compute $\overline{\Delta}$ and $\overline{\sigma}$ via Eq. (25), and compute the strain associated with that $\overline{\ell}_p$ via Eq. (24).

The stress–strain state at the completion of yielding is simply $\overline{\ell}_p \to 1/4$. The composite stress and strain at the completion of full yielding is given by

$$[\overline{\epsilon}_c,\overline{\sigma}_c]_{fy} = \left[\frac{\Sigma_Y}{2\kappa_2^2}\left(\frac{1}{2}+\frac{5\kappa_2}{8}+\cosh\frac{\kappa_2}{2}\right), \frac{\Sigma_Y}{4}\right] \tag{31}$$

This result confirms the elementary equilibrium result for the composite stress if the interface has experienced complete yielding. Finally, one can show that the composite stress for initial yielding is always smaller than that at complete yielding: this means that the propagation of the plastic zone implies strain hardening of the material, or stable propagation of the plastic zone with increasing applied strain. This is a purely geometry effect, as opposed to a fundamental physical mechanism in either constituent material. The plastic zone initiates at the brick corners and propagates inwards: the plastic zone in effect shields the inner elastic core, such that higher loads are required to continue to propagate the plastic zone.

The peak shear strain at the edge of the plastic zone at the completion of yielding is given by

$$(\overline{\gamma}_{max})_{fy} = \frac{\Sigma_Y}{2\kappa_2^2}\left(\frac{1}{2}+\frac{\kappa_2^2}{16}+\frac{1}{2}\cosh\left[\frac{\kappa_2}{2}\right]\right) \tag{32}$$

If this value is less than the shear rupture strain for the mortar, one can neglect the possibility of mortar rupture during propagation of the plastic zone. Again, note that the normalized shear yield strain is given by $\overline{\gamma}_Y = \Sigma_Y/(2\kappa_2^2)$, such that $(\overline{\gamma}_{max})_{fy}$ value is always greater than $\overline{\gamma}_Y$ for any value of κ_2. This means that the shear strain at the edge of the plastic zone always increases during propagation of the plastic zone.

3.4. Composite rupture via shear failure

After complete yielding, the stress is fixed to be constant, i.e. $\overline{\sigma}_c = \Sigma_Y/4$, and one must solve for the composite strain associated with rupture of the horizontal interface. After complete yielding, an increment in applied strain, $d\epsilon_c$, results in a rigid-body translation of the top brick, $du_r = w\cdot d\epsilon_c/2$. This causes an increment in the total shear strain (along the entire interface) of $d\gamma = du_r/t$. Thus, the increment in shear strain is $d\overline{\gamma} = d\overline{\epsilon}_c/2$. Using the state at the completion of yielding as a reference, the total shear strain is given by

$$\overline{\gamma}_{max} = (\overline{\gamma}_{max})_{fy} + \tfrac{1}{2}(\overline{\epsilon}_c - (\overline{\epsilon}_c)_{fy}) \tag{33}$$

Equating this to the shear rupture strain of the mortar yields the following for the critical composite strain associated with failure. Here, we define the rupture strain of the mortar as $\overline{\gamma}_R \equiv \overline{\gamma}_Y(1+r)$, where r reflects the amount of plastic shear strain (that beyond the initial yield strain) required for rupture, normalized by the initial yield strain. Thus, the final state of the material is given by

$$[\overline{\epsilon}_c,\overline{\sigma}_c]_R = \left[\frac{\Sigma_Y}{\kappa_2^2}\left(1+r+\frac{1}{4}\kappa_2^2\right), \frac{\Sigma_Y}{4}\right] \tag{34}$$

Note that this equation is only to be applied provided that r is large enough to ensure that failure does not occur during propagation of the plastic zone.

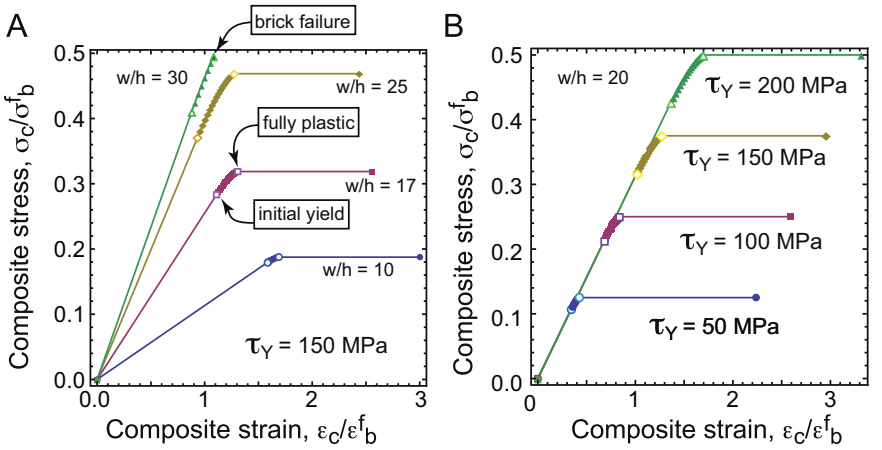

Fig. 6. Elastic–plastic stress–strain curves for composites with pre-cracked vertical interfaces: in part (A) results are shown for $w/h=10$, 17, 25, 30, with $\tau_Y=150$, $\gamma_R=\gamma_Y+0.005$, $E_m=4$ GPa, $E_b=300$ GPa, $h=1$ μm, $t=0.5$ μm, and $\epsilon_b^f=1/300$. In part (B), results are shown for $t=0.5$ μm, $\gamma_R=0.2$, $w/h=20$, and $\tau_Y=50, 100, 150, 200$ MPa. The data points are the result of the numerical solution to the governing equations: note that the transition from initial yielding to complete yielding occurs over very small ranges of applied strain.

3.5. Examples of elastic–plastic stress–strain response and work of failure

Fig. 6 illustrates the composite stress–strain response that corresponds to the above predictions, for a representative polymeric mortar with the properties listed in the caption. (In these simulations, the vertical interfaces are assumed to carry no load.) The results illustrate the effect of brick aspect ratio (left) and mortar yield strength (right), with all other constituent properties fixed as indicated. The data points correspond to the numerical solution for the partial yield regime. It is clear that for small aspect ratios and low mortar yield strength, the applied strain range associated with propagation with the plastic zone is quite small. In these simulations, the rupture strain in the mortar is fixed to be $\gamma_R=\gamma_Y+0.005$, which dictates that the increment in composite strain required to rupture the composite is independent of the chosen yield stress.

Given that the transition from initial yielding to complete yielding of the horizontal interfaces occurs over very small strain increments, an accurate closed-form expression for the work of fracture (i.e. the area under the stress–strain curve) can be easily derived by defining the elastic limit as the intersection of the elastic response and the pull-out response. Here it is assumed that the bricks do not fail, such that Eq. (34) is satisfied: in this case, the work of fracture is given by

$$\overline{W}_f=\frac{2\overline{E}_b W_f}{(\sigma_b^f)^2}=\Sigma_Y\cdot\Gamma_R-\frac{\Sigma_Y^2}{8}\left(\frac{1}{\overline{E}_c}-1\right) \tag{35}$$

where $\Gamma_R=\gamma_R t/(\epsilon_b^f w)$. For simplicity's sake, assume that the rupture strain of the mortar is such that the first term dominates. In terms of constituent properties, the composite work of failure is given by

$$\overline{W}_f=\frac{\overline{E}_b\tau_Y}{(\sigma_b^f)^2}\cdot\frac{t}{h}=\frac{\overline{E}_b\tau_Y}{(\sigma_b^f)^2}\cdot\frac{f\cdot\overline{w}}{2+\overline{w}} \tag{36}$$

Thus, for fixed brick properties and fixed mortar volume fraction, the relative work to failure increases with increasing aspect ratio of the bricks—*provided brick failure does not occur*. This is simply because raising the aspect ratio of the bricks raises the pull-out stress, increasing the work to failure. Eventually, as the aspect ratio of the brick is increased for fixed mortar yield strength, the bricks will break, such that the above does not apply and the work to failure drops abruptly. Note also that, prior to brick failure, the work to failure is independent of the brick size for fixed mortar thickness: the small deviations from a constant value seen in Fig. 6 (prior to brick failure) are a result of the changing modulus, i.e. the terms neglected in Eq. (35).

4. Discussion

4.1. Brittle vertical interfaces and ductile horizontal interfaces

Fig. 7 summarizes the material response, assuming brittle vertical interfaces are governed by the failure strength $\sigma_i^f=\sqrt{3}\tau_Y$, where τ_Y is the yield stress of the horizontal interfaces. Fig. 7A illustrates the stress–strain predictions for several brick sizes and fixed interface strength: for short bricks, failure of the vertical interface controls strength, as the stress required for pull-out is beneath the stress required to break the vertical interfaces. However, as the bricks increase in size, the pull-out stress governs strength. If the bricks are too long ($w=40$ μm in this case), the pull-out stress is higher than the stress required to break the bricks, such that the composite fails before pull-out. The key characteristics of the

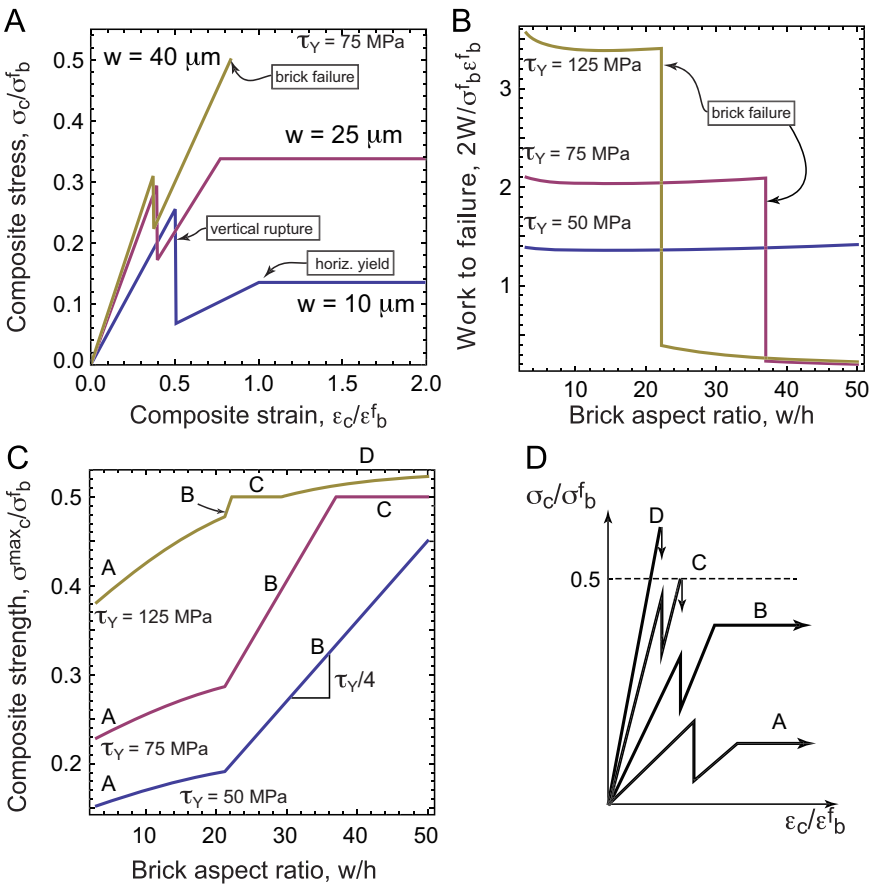

Fig. 7. (A) Illustrations of stress strain curves for various brick sizes and $\tau_Y = 75$ MPa, (B) failure work versus brick size, and (C) composite strength versus brick size. The assumed properties are $\tau_Y = 50, 75, 125$ MPa, with: $E_m = 3$ GPa, $t = 1$ μm, $h = 2$ μm, $E_b = 370$ GPa, $\sigma_b^f = 600$ MPa, and $\sigma_i^f = \sqrt{3}\tau_Y$, and $\gamma_R = 0.5$. The vertical interfaces are taken as brittle, such that vertical rupture occurs immediately upon reaching interface strength. Part (D) provides a schematic illustration of the four types of stress–strain response associated with each region labeled in Part (C).

stress–strain curve – work to failure, peak stress and modulus – are shown in Figs. 7B and C. The features of these curves can be understood in terms of the stress–strain response shown in Fig. 7A, and the failure sequence(s) outlined in Fig. 3.

For example, note the kink in the strength vs. brick size plot shown in Fig. 7C, which occurs near $w = 20$ μm; for smaller brick sizes, the vertical interface strength controls the peak stress (see result for $w = 10$ μm in Fig. 7A), while for large brick sizes, the pull-out stress controls peak stress (see result for $w = 25$ μm in Fig. 7A). After the kink, where pull-out stress controls the peak stress, the slope of the strength vs. brick sizes is proportional to the shear yield stress, as expected. The second kink, evidenced most clearly in the result for $\tau_Y = 75$ MPa in Fig. 7C, corresponds to brick failure: for bricks longer than ~ 37 μm, brick failure occurs prior to pull-out. This leads to an abrupt drop in failure work at this same critical brick size, as evidenced by the result in Fig. 7C. Note that for the strongest mortar, there is a very narrow range of brick sizes for which the pull-out stress governs peak stress and ductile behavior results, i.e. the small steep strain line just before the "ledge" in Fig. 7B. For the stiff mortar above brick sizes of ~ 29 μm, vertical interface failure again controls the composite strength, but the bricks fail immediately upon vertical interface rupture, such that the high strength region is associated with very brittle composite response.

Fig. 7A and d illustrates that vertical interfaces can have a profound effect on strength and modulus for small brick sizes, as expected. However, even for large aspect ratios, the vertical interface can play a critical role. For example, consider the case of $w/h = 10$: in all cases, the vertical strength is dictated by the vertical interfaces, and the modulus drops by a factor of two upon vertical cracking.

4.2. Optimal solutions

To simplify the discussion, consider the case of pre-cracked vertical interfaces. The optimal combination of mortar strength and brick geometry that maximizes strength is given by

$$\frac{\tau_Y w}{4\sigma_b^f h} = 1 \tag{37}$$

Very strong bricks relative to the mortar require large aspect ratios to optimize strength, while for very strong mortar, smaller aspect ratio bricks are required. Suppose that the mortar and brick strength are fixed, and the aspect ratio of the bricks is adjusted to maximize strength: in this case, and assuming the mortar is much weaker than the bricks, the composite work to failure is given by

$$\overline{W}_f = 4f \cdot \frac{\gamma_R}{\epsilon_b^f} \cdot \frac{\tau_Y}{\sigma_b^f} \tag{38}$$

Conversely, suppose the brick aspect ratio, $\overline{w}$, is fixed by the synthesis pathway, and the yield stress can be adjusted to maximize strength. The optimal work to failure is given by

$$\overline{W}_f = 4f \cdot \frac{\gamma_R}{\epsilon_b^f} \cdot \frac{2+\overline{w}}{\overline{w}^2} \tag{39}$$

In this case, small aspect ratio bricks are desired, assuming that one can increase the yield stress of the mortar to be close to that of bricks. This limit is not particularly meaningful, because it simply says that if you have ductile mortar that is of comparable strength to the bricks, one should simply make a material out of the mortar itself. Nevertheless, it does emphasize the fact that increases in mortar strength should be met with concomitant decreases in brick aspect ratio.

4.3. Materials comparison and implications for developments of synthetics

The present models create the opportunity to VET various potential brick and mortar composites by comparing their performance to existing materials. Clearly, the comparison should be made in the context of specific properties (i.e. properties divided by the density), as metals will generally be far stronger and more ductile in terms of raw properties, and typically much stiffer. Fig. 8 illustrates Ashby maps for modulus vs. failure work and failure work vs. strength, with all properties scaled by the density. Naturally, different applications require different scaling exponents, and the range of possible material properties is quite broad: however, the materials chosen in Fig. 8 are arguably representative of each class of material (ceramics, metals, polymers). Note that the log scale implies that a unit change in the figure corresponds to an order of magnitude, or a change of 0.3 corresponds to a factor of 2.

For reference, model predictions can be explicitly compared to measured properties of natural nacre and the nacre-inspired synthetic $Al_2O_3/PMMA$ composite of Munch et al. (2008). Using the properties from Table 2 for Alumina and PMMA, and the pertinent composite details from Munch et al. (2008) ($f=0.2$, $h=8$ μm, $w=50$ μm), Eq. (9) predicts a composite modulus of 122 GPa, very close to the measured value of 115 GPa (Munch et al., 2008). Using reasonable values for nacre ($E_m=100$ MPa, $E_b=100$ GPa, $f=0.025$, $h=0.2$ μm and $w=2$ μm, Jackson et al., 1988; Ji and Gao, 2004a), Eq. (9) predicts a modulus of 50 GPa, again very close to the measured value of 60 GPa (Jackson et al., 1988). For comparison, the model of Ji et al. predicts composite moduli of 30 GPa and 29 GPa for the synthetic composite and nacre, respectively (Ji and Gao, 2004a, Eq. (5)). The difference can be attributed to the effect of intact vertical interfaces, and highlights the importance of including such features when modeling this class of materials. Comparisons to other synthetic brick and mortar materials (e.g. Tang et al., 2003; Ekiz et al., 2009; Posiadlo et al., 2007; Bonderer et al., 2008, 2010a,b) are not appropriate here, since these materials have mortar volume fractions $\gg 40\%$. For such large volume fractions of mortar, the assumption of uniform mortar shear strain inherent to the present model is not valid and accurate predictions are not expected.

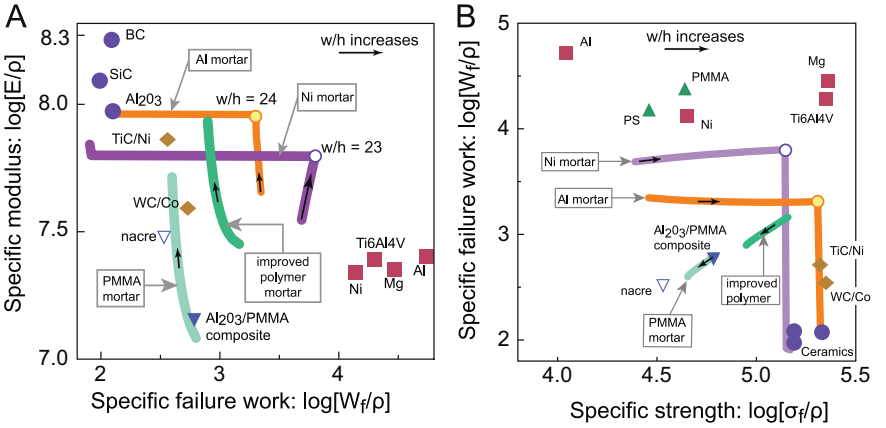

Fig. 8. Ashby property maps comparing the projected performance of various synthetic materials with ceramics, metals, polymers and cermets, with the assumed synthetic properties listed in Table 2. The micromechanical predictions are shown as thick lines, with the arrows indicating the direction of increasing aspect ratio w/h of the bricks. Note that the volume fraction of mortar varies along the prediction curves since the mortar thickness is held fixed as the brick size varies.

The map in Fig. 8 illustrates that natural nacre is a factor of 2–3 more ductile than engineered ceramics with a modulus that is 2–3 times smaller, yet slightly higher than metals. Nacre's specific strength compares favorably to pure heavy metals, but is almost an order of magnitude less strong than lightweight alloys. Interestingly, nacre has a comparable specific strength compared to plastics such as PS and PMMA, though it is more than 25 times stiffer. Nacre is clearly inspiring for its ability to achieve high ductility despite the fact it has a vanishing small fraction of ductile phase: in its raw form, however, it is not even close to being competitive with metals.

Interestingly, natural nacre has comparable (though not quite as good) specific work to failure, strength and modulus as engineered cermets such as TiC/Ni and WC/Co. This is noteworthy and inspiring, considering that the individual constituent properties of nacre are arguably not as impressive as these engineered metal/ceramics. *Clearly*, *this benefit is derived from a highly ordered microstructure.* The synthetic composite of *Munch et al.* provides an additional interesting comparison. It has $\sim 50\%$ the stiffness of natural nacre (due to a comparatively large polymeric volume fraction), but exhibits 50–100% more ductility, and twice the strength. The strength and ductility of the current ceramic/polymer synthetic outperforms cermets, with the exception of a lower modulus.

The potential of various ceramic/polymer and ceramic/metal synthetics is illustrated in Fig. 8 by showing results for various materials and varying brick size. First, consider a composite of identical composition to the aforementioned $Al_2O_3/PMMA$ material; using the properties given in Table 1, one predicts modulus, strength and ductility that is comparable to measurements in Espinosa et al. (2009) and Munch et al. (2008). Here, it assumed that the vertical interfaces are fully bonded, and experience rupture at $\sqrt{3}\tau_Y$, which is consistent with Von Mises plasticity. Further, the assumed brick strength and ductility of the PMMA mortar are likely significantly higher than reality; while brick strengths of 1.5 GPa are possible for small volume ceramics, they are at the upper ends of high quality ceramics. Similarly, the rupture strain of 150% is probably three times higher than conventional PMMA; one possible explanation is that friction remains high even after mortar rupture. The effect of increasing the brick length (while holding the brick thickness and mortar thickness fixed) is shown by the data points near the synthetic measurements. While the stiffness is considerably improved by increasing the brick size, the specific strength and work to failure actually decrease: this is a consequence of the decreasing volume fraction of mortar, which has a much lower density than the ceramic (about a factor of three). That is, the raw strength and work to failure go up for longer bricks, but the penalty associated increasing density is larger than the benefit. Note that for the range of constituent properties considered here, no transitions in failure mechanism are observed for brick lengths in the range of $5-50\ \mu m$.

Ceramic/polymer brick and mortar structures can be considerably improved if the yield stress of the polymer mortar can be increased by 50% (to ~ 150 MPa), as indicated by the lines labeled "improved composite". Basically, increasing the

Table 1
Properties chosen for existing materials.

Material	Modulus (GPa)	Yield stress/strength (MPa)	Failure strain (–)	Density (g/cm^3)
Ceramics				
SiC	400	500	0.0013	3.2
Al_2O_3	370	600 (bulk)	0.0016	3.9
BC	450	530	0.0012	2.5
Metals				
Ni	200	100	0.5	8.9
Al	70	100	0.2	2.7
Mg alloy	45	400	0.14	1.9
Ti6Al4V	110	830	0.11	4.4
Cermets				
TiC/Ni	445	1500	0.0031	6.0
WC/Co	580	3500	0.0052	14.4
Polymers				
PS	2	30	0.55	1.0
PMMA	2	50	0.6	1.2

Table 2
Properties chosen for candidate composites.

Material	Modulus (GPa)	Yield stress (MPa)	Failure strain (–)	Density (g/cm^3)	Thickness (μm)
Al_2O_3 bricks	370	1500 (small vol.)	0.004	3.9	2 for Ni, 5 for others
PMMA mortar	2.5	100 or 150	1.5	1.2	1
Ni mortar	200	100	0.5	8.9	1
Al mortar	70	150	0.2	2.7	1

yield strength allows for more efficient transfer of loads to the bricks, driving up the modulus, strength and work to failure. Though such composites would not be competitive with metals (based on just this comparison), such materials would be an order of magnitude stronger and more ductile than ceramics, yet have comparable modulus. In order to realize this gain, the critical challenge that must be addressed is a synthesis pathway for making strong, long bricks measuring roughly five by fifty microns. Smaller bricks with thinner mortar sections would serve just as well, but would likely create significant synthesis challenges: merely decreasing the mortar thickness serves no purpose, as the mortar volume fraction decreases as well, limiting ductility (as indicated by Eq. (41)).

Arguably the greatest opportunity for new high-performance materials is the exploitation of ductile metal mortar. Theoretical material responses are shown in Fig. 8 for pure nickel and pure aluminum mortar, with rupture strains of 0.5 and 0.2, respectively. Properties for these materials are widely variable, and values were specifically chosen to be reasonable while leading to very different predictions. The abrupt shift in the curves is associated with the transition to brick failure: eventually as the brick size is increased, bricks fail prior to pull-out and the work-to-failure drops abruptly. The critical brick size for the aluminum mortar associated with failure is 42 μm, while that for the nickel mortar is 24 μm. This difference is attributable to the difference in elastic modulus. A comparison of the nickel and aluminum mortar predictions illustrates the role of the mortar modulus, and bonding of the vertical interfaces: the nickel predictions assume that the vertical interface strength is $\tau_Y/10$, while the aluminum predictions assume vertical interface strengths of $\sqrt{3}\tau_Y$: these assumptions are motivated by the presumption that alumina/aluminum bonding will be stronger than that of alumina/nickel. Clearly, much more detailed study is needed with the present model to understand trade-offs between mortar modulus, strength and brick size. It is worth noting that the concept of metallic mortar is currently under development (Launey et al., 2010), but as of yet, the metallic mortar volume fraction is too high to realize the gains seen in Fig. 8.

5. Conclusions

- For synthetic materials with strong mortar/brick bonding, the vertical interfaces play an important role in contributing to the overall composite stiffness; for short bricks, the vertical interfaces also play a significant role in raising the peak strength of the composite.
- The peak strength, stiffness and work-to-failure of the material are optimized when the geometry is tuned to an optimal brick size for a given mortar yield strength, or vice versa: increasing the mortar yield strength decreases the optimal brick size.
- The principle gain of these materials over existing alloys is to maintain the stiffness of a ceramic while dramatically increasing the work-to-failure over ceramics. Existing polymer/ceramic synthetics are competitive with cermets with regard to modulus and work to failure, with smaller strengths. Materials optimization to increase mortar strength and brick size will lead to high strength polymer/ceramic composites that exceed cermets. This is encouraging in the sense that cemented carbides represent one extreme of the brick-and-mortar design space (i.e. high interface strength and high mortar strength), with gains resulting from ceramic alignment.
- The use of metallic mortar material can dramatically increase the strength and work to failure of the brick and mortar composites, leading to true outliers that defeat the general trend of decreasing failure work with increasing modulus exhibited by current materials. The higher strength and stiffness of metallic mortar would also decrease the desired brick aspect ratio, which would likely mitigate synthesis challenges.
- Though not considered here, the role of constrained plasticity in the vertical interfaces and any subsequent ductile straining of vertical interfaces could lead to even more dramatic improvements in brick and mortar materials.

Acknowledgments

The work of M.R.B., N.R.P. and B.G.C. was supported by the Institute for Collaborative Biotechnologies through contract no. W911NF-09-D-0001 from the U.S. Army Research Office. Additional support for M.R.B. was provided by the NSF CMII, through Grant #1063714 (formally Grant #0800790). The involvement of R.O.R. was supported by the Office of Science, Office of Basic Energy Sciences, Division of Materials Sciences and Engineering, of the U.S. Department of Energy under Contract no. DE-AC02-05CH11231.

References

Barthelat, F., Li, C.-M., Comi, C., Espinosa, H.D., 2006. Mechanical properties of nacre constituents and their impact on mechanical performance. J. Mater. Res. 21, 1977–1986.

Barthelat, F., Tang, H., Zavattieri, P.D., Li, C.-M., Espinosa, H.D., 2007. On the mechanics of mother-of-pearl: a key feature in the material hierarchical structure. J. Mech. Phys. Solids 55, 306–337.

Bonderer, L.J., Studart, A.R., Gauckler, L.J., 2008. Bioinspired design and assembly of platelet reinforced polymer films. Science 319, 1069.

Bonderer, L.J., Feldman, K., Gauckler, L.J., 2010a. Platelet-reinforced polymer composites by combined gel-casting and hot-pressing. Part I: polypropylene matrix composites. Compos. Sci. Technol. 70, 1958–1965.

Bonderer, L.J., Feldman, K., Gauckler, L.J., 2010b. Platelet-reinforced polymer composites by combined gel-casting and hot-pressing. Part II: thermoplastic polyurethane matrix composites. Compos. Sci. Technol. 70, 1966–1972.
Currey, J.D., Zioupos, P., Davies, P., Casinos, A., 2001. Mechanical properties of nacre and highly mineralized bone. Proc. R. Soc. London B 268, 107–111.
Ekiz, O.O., Dericioglu, A.F., Kakisawa, H., 2009. An efficient hybrid conventional method to fabricate nacre-like bulk nano-laminar composites. Mater. Sci. Eng. C 29, 2050–2054.
Espinosa, H.D., Rim, J.E., Barthelat, F., Buehler, M.J., 2009. Merger of structure and material in nacre and bone—perspectives on de novo biomimetic materials. Prog. Mater. Sci. 54, 1059–1100.
Evans, A.G., Suo, Z., Wang, R.Z., Akay, L.A., He, M.Y., Hutchinson, J.W., 2001. Model for the robust mechanical behavior of nacre. J. Mater. Res. 16, 2475–2484.
Gao, H., Ji, B., Jager, I.L., Arzt, E., Fratzl, P., 2003. Materials become insensitive to flaws at nanoscale: lessons from nature. Proc. Natl. Acad. Sci. 100, 5597–5600.
Hu, M.S., Evans, A.G., 1989. The cracking and decohesion of thin films on ductile substrates. Acta Metall. Mater. 37, 917–925.
Jackson, A.P., Vincent, J.F.V., Turner, R.M., 1988. The mechanical design of nacre. Proc. R. Soc. London B 234, 415–440.
Jager, I., Fratzl, P., 2000. Mineralized collagen fibrils: a mechanical model with a staggered arrangement of mineral particles. Biophys. J. 79, 1737–1746.
Ji, B., Gao, H., 2004a. Mechanical properties of nanostructure of biological materials. J. Mech. Phys. Solids 52, 1963–1990.
Ji, B., Gao, H., 2004b. A study of fracture mechanisms in biological nano-composites via the virtual internal bond model. Mater. Sci. Eng. A 366, 96–103.
Kakisawa, H., Sumitom, T., Inoue, R., Kagawa, Y., 2010. Fabrication of nature-inspired bulk laminar composites by a power processing. Compos. Sci. Technol. 70, 161–166.
Launey, M.E., Munch, E., Alsem, D.H., Barth, H.B., Saiz, E., Tomsia, A.P., Ritchie, R.O., 2009. Designing highly toughened hybrid composites through nature-inspired hierarchical complexity. Acta Mater. 57, 2919–2932.
Launey, M.E., Munch, E., Alsem, D.H., Saiz, E., Tomsia, A.P., Ritchie, R.O., 2010. A novel biomimetic approach to the design of high-performance ceramic–metal composites. J. R. Soc. Interface 7, 741–753.
Munch, E., Launey, M.E., Alsem, D.H., Saiz, E., Tomsia, A.P., Ritchie, R.O., 2008. Tough, bio-inspired hybrid materials. Science 322, 1516–1519.
Nairn, J.A., 1997. On the use of shear-lag methods for the analysis of stress transfer in unidirectional composites. Mech. Mater. 26, 63–80.
Posiadlo, P., Kaushik, A.K., Arruda, E.M., Waas, A.M., Shim, B.S., Xu, J., Nandivada, H., Pumplin, B.G., Lahann, J., Ramamoorthy, A., Kotov, N.A., 2007. Ultrastrong and stiff layered polymer nanocomposites. Science 318, 80.
Rabiei, R., Bekah, S., Barthelat, F., 2010. Failure mode transition in nacre and bone-like materials. Acta Biomater. 6, 4081–4089.
Tang, Z., Kotov, N.A., Magonov, S., Ozturk, B., 2003. Nanostructured artificial nacre. Nat. Mater. 2, 413–418.
Tang, H., Barthelat, F., Espinosa, H.D., 2007. An elasto-viscoplastic interface model for investigating the constitutive behavior of nacre. J. Mech. Phys. Solids 55, 1410–1438.
Tucker, C.L., Liang, E., 1999. Stiffness predictions for unidirectional short-fiber composites: review and evaluation. Compos. Sci. Technol. 59, 655–671.
Wang, L., Boyce, M.C., 2010. Bioinspired structural material exhibiting post-yield lateral expansion and volumetric energy dissipation during tension. Adv. Functional Mater. 20, 3025–3030.
Wilbrink, D.V., Utz, M., Ritchie, R.O., Begley, M.R., 2010. Scaling of strength and ductility in bio-inspired brick and mortar composites. Appl. Phys. Lett. 97, 193701.
Zhang, Z., Zhang, Y.-W., Gao, H., 2011. On optimal hierarchy of load-bearing biological materials. Proc. R. Soc. B 78, 519–525.
Zhang, Z.Q., Liu, B., Huang, Y., Hwang, K.C., Gao, H., 2010. Mechanical properties of unidirectional nanocomposites with non-uniformly or randomly staggered platelet distribution. J. Mech. Phys. Solids 58, 1646–1660.